

*Supporting Information for*

**Oxygen Sensitivity of [FeFe] Hydrogenases: A Comparative Study of Active Site Mimics Inside vs Outside the Enzyme**

Shanika Yadav, Rieke Haas, Esma Birsen Boydas, Michael Roemelt, Thomas Happe, Ulf-Peter Apfel and Sven T. Stripp

**Contents**

Experimental methodology

Computational methodology

- Figure S1 Molecular structures of the  $\text{Fe}_2(\text{adt}^{\text{Cbz}})(\text{CO})_6$  intermediate
- Figure S2 FTIR spectra of  $\text{Fe}_2(\text{adt}^{\text{Cbz}})(\text{CO})_6$  and  $\text{Fe}_2(\text{adt})(\text{CO})_6$
- Figure S3 Schematic representation of the modified synthesis
- Figure S4 FTIR spectra of  $\text{ADT}_{\text{CN}}$  [1] and  $\text{PDT}_{\text{CN}}$  [2] upon  $\text{O}_2$  purging
- Figure S5 FTIR spectra of  $\text{ADT}_{\text{monoCN}}$  [3] and  $\text{PDT}_{\text{monoCN}}$  [4] upon  $\text{O}_2$  purging
- Figure S6 FTIR spectra of  $\text{ADT}_{\text{CN}}$  [1] +  $\text{CH}_3\text{COOH}$  and  $\text{PDT}_{\text{CN}}$  [2] +  $\text{CH}_3\text{COOH}$
- Figure S7 FTIR spectra of  $\text{ADT}_{\text{CN}}$  [1] +  $\text{TsOH}$  and  $\text{PDT}_{\text{CN}}$  [2] +  $\text{TsOH}$
- Figure S8 FTIR spectra of  $\text{ADT}_{\text{CN}}$  [1] +  $\text{H}_2\text{O}_2$  and  $\text{PDT}_{\text{CN}}$  [2] +  $\text{H}_2\text{O}_2$
- Figure S9 Mössbauer spectra of  $\text{ADT}_{\text{CN}}$  [1] +  $\text{H}_2\text{O}_2$  and  $\text{PDT}_{\text{CN}}$  [2] +  $\text{H}_2\text{O}_2$
- Figure S10 Reactivity of *CrHydA1* cofactor variants activated with  $\text{ADT}_{\text{CN}}$  [1] or  $\text{PDT}_{\text{CN}}$  [2].
- Figure S11 Reactions of *CrHydA1* cofactor variants  $\text{ADT}$ -monoCN [3] or  $\text{PDT}$ -monoCN [4]
- Figure S12 Protonation changes in *CrHydA1* wildtype ( $\text{ADT}_{\text{CN}}$ ) and cofactor variant  $\text{PDT}_{\text{CN}}$ .
- Figure S13-14 Possible isomers of  $\text{ADT}_{\text{CN}}$  [1] and  $\text{PDT}_{\text{CN}}$  [2]
- Figure S15-17 Relative Gibbs energies of isomers of  $\text{ADT}_{\text{CN}}$  [1],  $\text{PDT}_{\text{CN}}$  [2] and  $\text{ADT}$ -monoCN [3]
- Figure S18 Spin isodensity plots
- Figure S19-20 Oxygenation reaction coordinate for  $\text{XDT}_{\text{CN}}$
- Figure S21 Reactions of the incoming oxygen and the bridgehead proton in  $\text{ADT}_{\text{CN}}$  [1]
- Figure S22 Calculated IR spectra for  $\text{ADT}_{\text{CN}}$  [1] and  $\text{PDT}_{\text{CN}}$  [2]
- Figure S23 Correlation graph (exp./cal.) for  $\text{ADT}_{\text{CN}}$  [1] and  $\text{PDT}_{\text{CN}}$  [2]

Table S1–S7

References

## Experimental methodology

Starting materials and chemicals were obtained from commercial suppliers and used without further purification - potassium superoxide, hydrogen peroxide (30% w/w in water), *p*-toluene sulphonic acid (TsOH) were purchased from Sigma-Aldrich. 18-crown-6-ether was obtained from TCI chemicals. Thiol - adt<sup>Cbz</sup> was synthesized according to the previously reported procedure.<sup>[1]</sup> Molecular oxygen (99.9%) was obtained from Air Liquide. All solvents were dried and degassed according to standard methods.<sup>[2]</sup>

For the spectroscopic measurements, all manipulations were carried inside an argon filled glovebox. All solutions were freshly prepared prior to experiments. Oxygen was introduced into the sample by purging the solutions with O<sub>2</sub> gas out of the glovebox. Other oxidizing agents (if stored outside the glovebox) were degassed before experiments by purging with argon for 15 minutes.

ATR FTIR spectra were recorded at Shimadzu Tracer 100 FT-IR. The synthesized complexes were measured as thin films dried from an appropriate solution on the Ge crystal. The observed absorption bands are given in wavenumbers (cm<sup>-1</sup>) and the intensity is described as weak (w), medium (m), strong (s) or very strong (vs) and their shape as broad (br) or shoulder (sh). For oxidation studies, the FTIR spectra were recorded with a MCT detector at 2 cm<sup>-1</sup> resolution. Sample solution was prepared in gastight vials and measured in a Specac liquid IR cell with CaF<sub>2</sub> windows of 0.05 mm pathlength. The concentration of the samples was 50 mM in dry MeCN. For experiments with O<sub>2</sub>, the samples were brought out of the glovebox in septum-sealed vials and purged with O<sub>2</sub> for 30 seconds. Experiments with 30% H<sub>2</sub>O<sub>2</sub> were performed by addition of specific equivalents to the complex solutions via gas tight syringes.

*In situ* ATR FTIR spectroscopy was performed on a Bruker Tensor27 with a Smith Detection ATR unit as described previously.<sup>[3]</sup> The protein samples were measured under a protective N<sub>2</sub>/H<sub>2</sub> atmosphere (98:2) within a Coy Lab anaerobic chamber with 8 scans per measurement and a spectral resolution of 2 cm<sup>-1</sup>. For each measurement, 5 μL of the protein sample was placed on the ATR crystal, closed with custom designed gas-tight lid and dried over a N<sub>2</sub> gas stream (5 L/min) for 10 to 30 min. To oxidise the samples, 20% O<sub>2</sub> or 5% H<sub>2</sub>O<sub>2</sub> was introduced.

NMR spectra were recorded at room temperature on a Bruker Advanced-400 NMR spectrometer (<sup>1</sup>H 400 MHz) and the shifts are reported in parts per million (ppm) relative to the solvent peaks of the deuterated solvent. The concentration of the samples was 50 mM in dry d<sub>3</sub>MeCN and samples were prepared in J. Young NMR tubes inside the glovebox.

Zero-field Mössbauer spectra were recorded by using a constant acceleration spectrometer equipped with a temperature controller maintaining temperatures within ±0.1 K and a <sup>57</sup>Co radiation source in a Rh matrix. Isomer shifts are referred to α-Fe metal at room temperature.

Data were fit with a sum of Lorentzian quadrupole doublets by using a least - square routine with WMOSS program. All spectra were recorded as solution in acetonitrile in a plastic sample holder which was frozen in liquid nitrogen. The samples were measured at 80 K and data were accumulated for about 18 to 24 hours.

All protein sample were prepared according to standard procedure.<sup>[4]</sup> CrHyA1 variants were incubated with a 5-fold molar excess of model complexes in 100 mM potassium phosphate buffer (Kpl), pH 6.8, containing 2 mM sodium dithionite (NaDT) for 30 min at 25°C. Subsequently, the holo-enzymes were purified by chromatography to remove excess complexes and concentrated to 50  $\mu$ M to 1 mM and stored at  $-80^{\circ}$ C in 100 mM Tris/HCl buffer pH 8.0 with 2 mM NaDT.

## Computational Methodology

Geometry optimizations by means of DFT and broken-symmetry DFT were carried out with the ORCA program package in its version 5.0.3.<sup>[9]</sup> The global hybrid B3LYP functional<sup>[10]</sup> along with ma-ZORA-def2-TZVP<sup>[11]</sup> basis set were used in the structure optimizations. Grimme's semi empirical van der Waals corrections with the Becke-Johnson damping (D3BJ) was incorporated for dispersive and non-covalent interactions. Scalar relativistic effects were approximated by means of zeroth order regular approximation (ZORA).<sup>[12-14]</sup> The resolution-of-identity in conjunction with chain-of-spheres algorithms (COSX) were used to expedite the computation of two-electron integrals during SCF cycles while SARC/J basis was employed as an auxiliary basis.<sup>[15-20]</sup> Solvent effects were taken into account in an implicit manner, utilizing Conductor-like Polarizable Continuum model (C-PCM). All structures were fully optimized without symmetry constraints. Normal mode analysis was performed to identify the nature of the ground- and transition-state structures. Free energies were reported in kcal/mol at 1 atm and 298 K. Two distinct reaction profiles have been documented for the oxygenation reaction mechanism: one involving infinitely separated reactants as the reference system (**Figure S19**), and the other characterized by the presence of pre-reactive complexes (PRCs) (**Figure S20**). The formation of pre-reactive complexes involving **[1]** + O<sub>2</sub> occurred by placing the O<sub>2</sub> moiety approximately 3 angstroms away from the substrate in the initial geometry, followed by complete optimization of this arrangement to establish a van der Waals complex.

A scaling factor of 0.978 for the calculated IR frequencies has been obtained through comparison of calculated vs. experimental IR CO and CN vibrations of the initial state of the substrate. See the Vibrational Spectra section for more information.

## Electronic structure of the substrates in the initial state

*Structural parameters.* Initial states of complexes **[1]** and **[2]** with two antiferromagnetically coupled local spins leading to a spin singlet was modelled by means of broken symmetry DFT. Loewdin spin populations targeting the aforementioned states are given in the following table.

Loewdin spin populations of the most stable isomers for ADT<sub>CN</sub> **[1]** and PDT<sub>CN</sub> **[2]** from BS-DFT targeting an antiferromagnetically coupled Fe(I) dimer.

	ADT <sub>CN</sub> <b>[1]</b>	PDT <sub>CN</sub> <b>[2]</b>
Fe	-0.6035	-0.5832
Fe	0.6121	0.5949

## Kinetic and thermodynamic analysis

*Initial state.* Five structural isomers which differ in apical and basal ligand positions were taken into account as shown in **Figures S13–S14**. All isomers were found to be isoenergetic (relative Gibbs free energies within 1 kcal/mol). However, the ligand arrangement around the iron centers displayed a noticeable change in the IR spectra in terms of relative intensities of CO vibrations. The Fe(I)-Fe(I) distance in all isomers in both ADT<sub>CN</sub> and PDT<sub>CN</sub> sets was found to be around 2.83 Å. The ligands adjacent to the bridge are capable of forming a weak hydrogen bonding with the pendant proton, at angles at around approximately 70 degrees and at distances around 2.6 and 2.9 Å for CN and CO moieties, respectively.

In addition to apical-basal structural isomerism, a CO-bridged intermediate with an open coordination site in one of the Fe(I) units was also located. The relative Gibbs free energies for these isomers are given in **Figures S15–S17**. Creating a CO bridge introduces a strain to the initial state of the hydrogenase mimic, which comes with an energy penalty of around 11-12 kcal/mol.

To check the feasibility of abstracting the bridgehead proton by the adjacent cyanide group, the corresponding CNH-product has been located and is shown in Figure S22. It has a relative energy of 47.2 kcal/mol relative to the initial state of the substrate, and therefore found to be thermodynamically unfeasible.

For the ADT<sub>mono</sub> complex, five candidates for the initial state have been considered regarding the ligation of CN group. Similar to other complexes, the apical-basal isomerism of CN<sup>-</sup> resulted in isoenergetic complexes, and the CO-bridged complex was around 11.4 kcal/mol less stable due to the aforementioned strain brought by the bridging CO.

## Figures

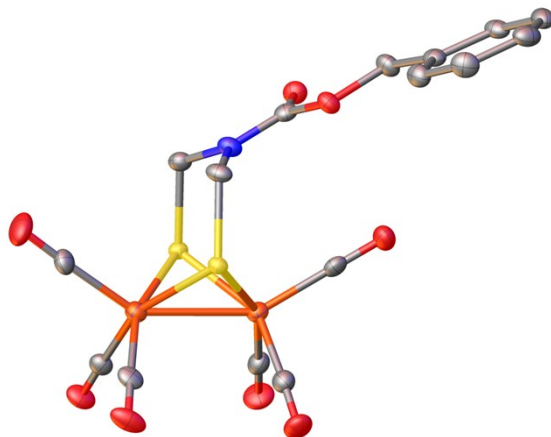


**Figure S1** | Molecular structures of the  $\text{Fe}_2(\text{adt}^{\text{Cbz}})(\text{CO})_6$  intermediate shown with thermal ellipsoid drawn 50% probability level. Hydrogen atoms are omitted for clarity, color code: grey-carbon, blue-nitrogen, yellow-sulfur, red-oxygen, orange-iron.

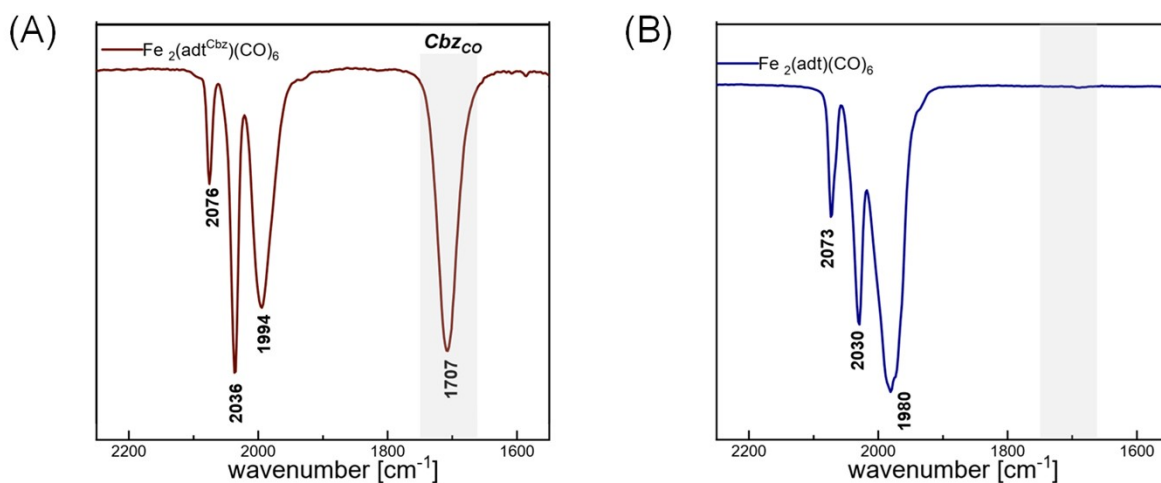


**Figure S2** | FTIR spectra of  $\text{Fe}_2(\text{adt}^{\text{Cbz}})(\text{CO})_6$  (red trace) and  $\text{Fe}_2(\text{adt})(\text{CO})_6$  (blue trace) in the CO region. The grey box highlights the loss of 1707  $\text{cm}^{-1}$  signal. The later represents the C=O vibration of the amine bond that is lost upon cleavage of the benzyl carbamate group (cbz, see Fig. S1).

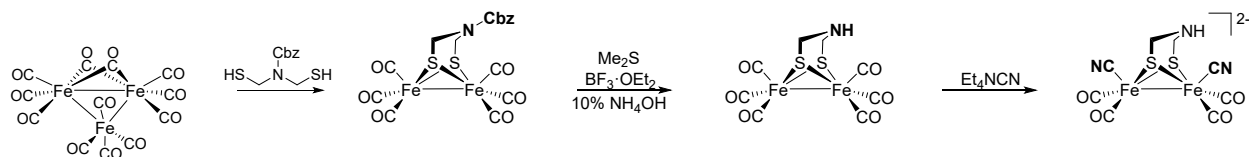


**Figure S3** | Schematic representation of the modified synthesis towards complex [1] via  $\text{Fe}_2(\text{adt}^{\text{Cbz}})(\text{CO})_6$ .

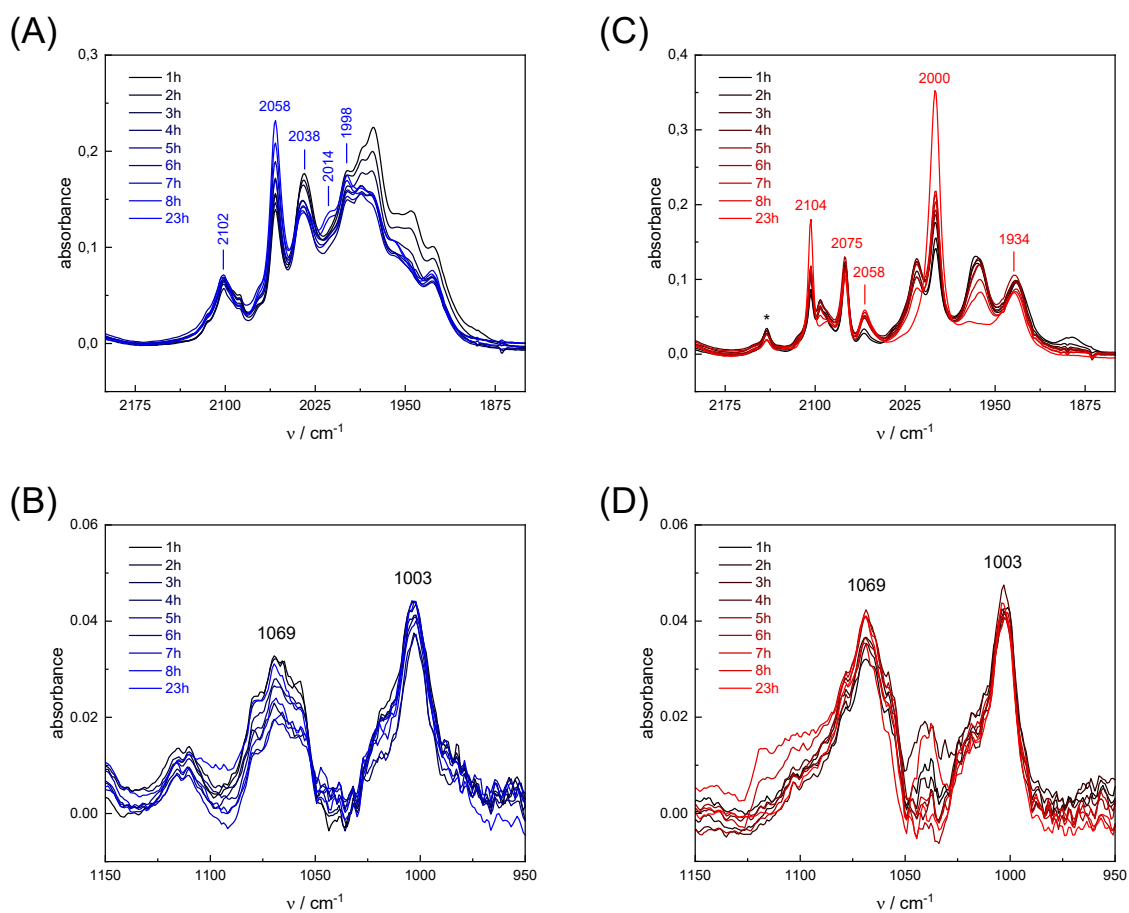


**Figure S4** | FTIR spectra of  $\text{ADTCN}$  [1] and  $\text{PDTCN}$  [2] upon  $\text{O}_2$  purging recorded at an interval of 60 minutes up to 8 hours and thereafter at 23 hours. Panels (A) and (C) depict the CO- and CN-vibrations of the complexes, panels (B) and (D) the low frequency end of the spectrum where S=O bonds may absorb. More prominent bands at  $1069\text{ cm}^{-1}$  and  $1003\text{ cm}^{-1}$  do not show significant changes between 1–23 h.

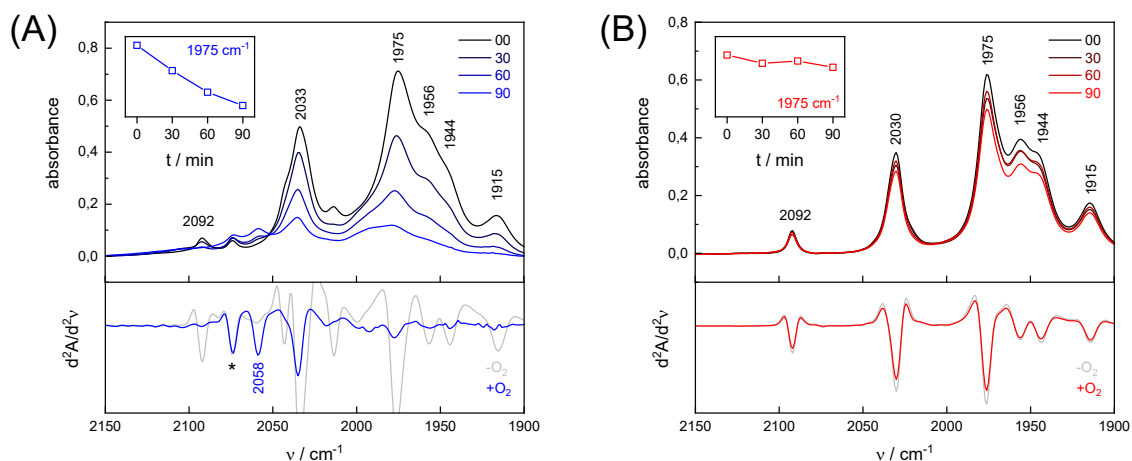


**Figure S5** | FTIR spectra of ADT<sub>monoCN</sub> [3] (A) and PDT<sub>monoCN</sub> [4] (B) upon O<sub>2</sub> purging displayed at an interval of 30 minutes. The asterisk marks an unchanging solvent band.

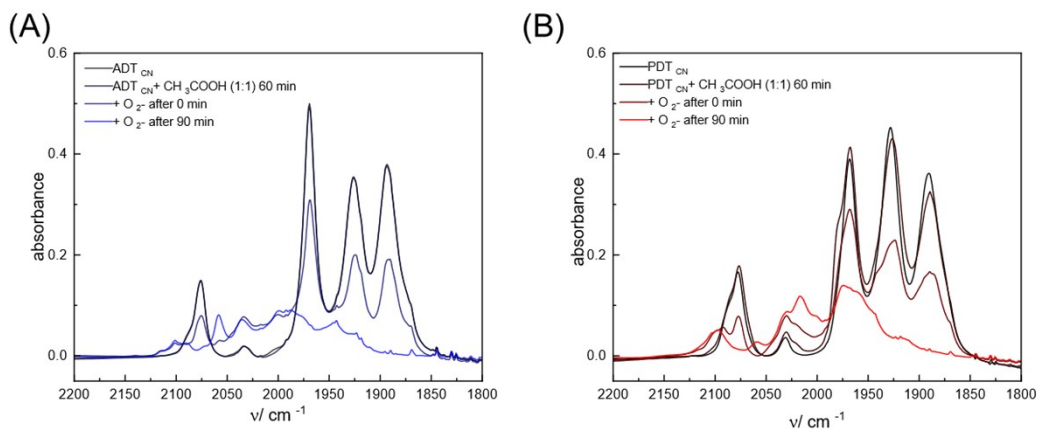


**Figure S6** | FTIR spectra of ADT<sub>CN</sub> [1] (A) and PDT<sub>CN</sub> [2] (B) after introduction of 1 equivalent CH<sub>3</sub>COOH. Thereafter, the FTIR spectra recorded for both complex solutions after purging with O<sub>2</sub> at an interval of 90 minutes.

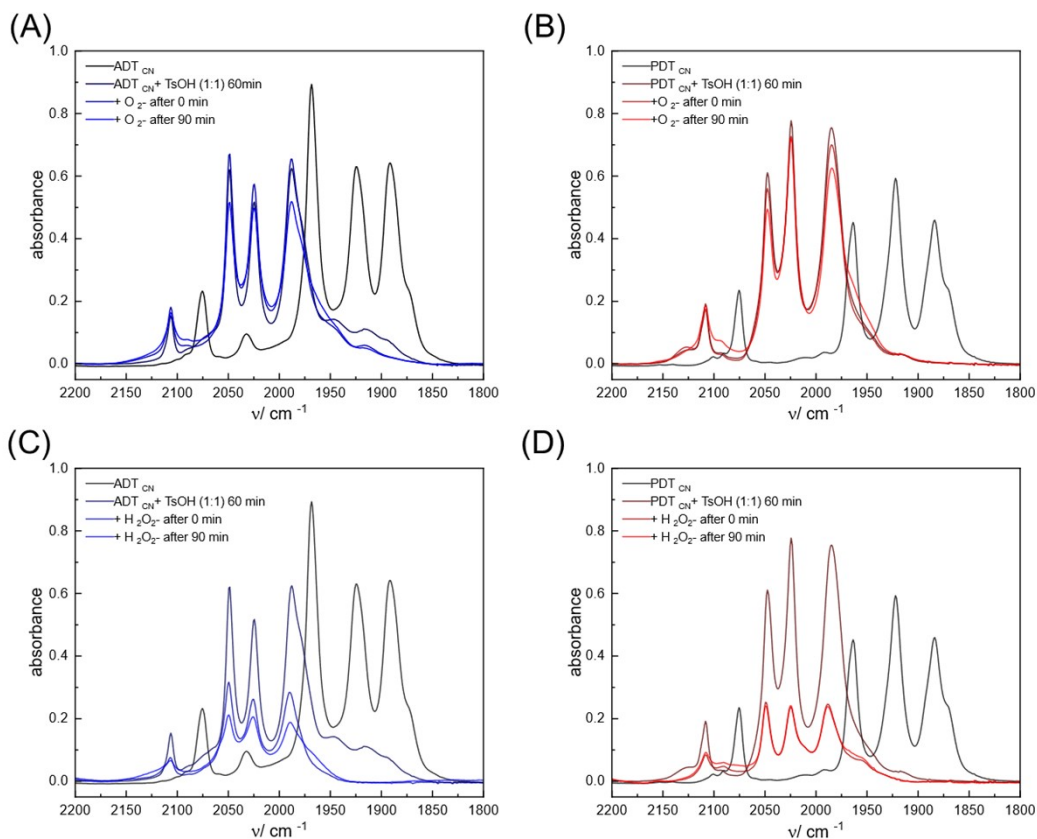


**Figure S7** | FTIR spectra of ADT<sub>CN</sub> [1] (A) and PDT<sub>CN</sub> [2] (B) after introduction of 1 equivalent TsOH. Thereafter, the FTIR spectra recorded after purging with O<sub>2</sub> at an interval of 90 minutes, indicating oxygen resistance. FTIR spectra of ADT<sub>CN</sub> [1] on reaction with 4 equivalents of H<sub>2</sub>O<sub>2</sub> in presence of TsOH (C) and PDT<sub>CN</sub> [2] on reaction with 8 equivalents of H<sub>2</sub>O<sub>2</sub> in presence of TsOH (D). Different equivalents of H<sub>2</sub>O<sub>2</sub> were used for the two complexes as in absence of TsOH, ADT<sub>CN</sub> reacts with lesser equivalents of H<sub>2</sub>O<sub>2</sub> while PDT<sub>CN</sub> requires comparatively more equivalents of H<sub>2</sub>O<sub>2</sub> to show reactivity.

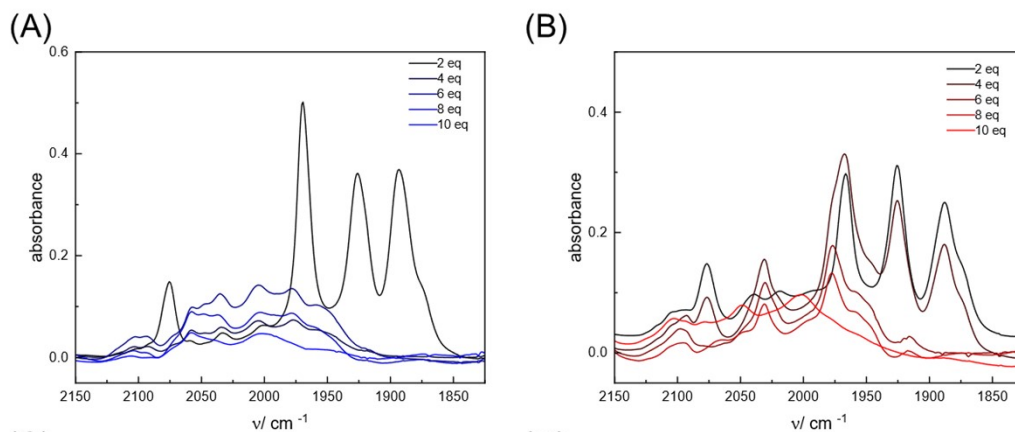


**Figure S8** | FTIR spectra of ADT<sub>CN</sub> [1] with different equivalents of H<sub>2</sub>O<sub>2</sub> (A) and PDT<sub>CN</sub> [2] with different equivalents of H<sub>2</sub>O<sub>2</sub> (B).

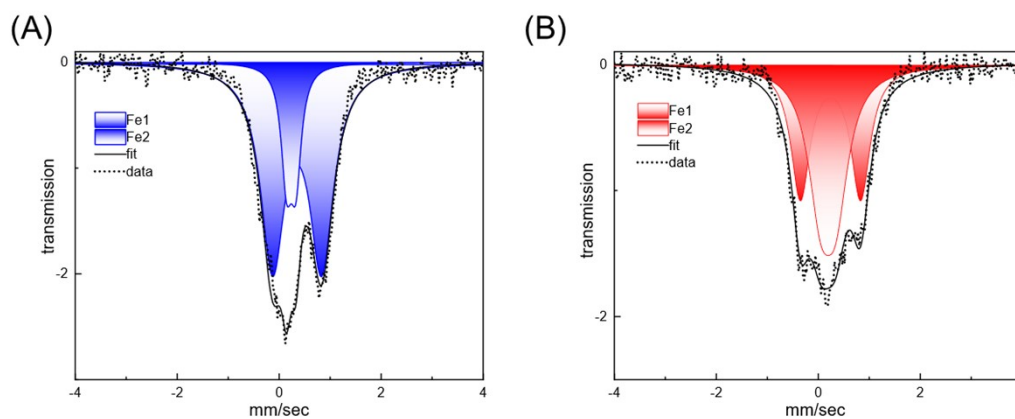


**Figure S9** | Mössbauer spectra of ADT<sub>CN</sub> [1] + 8 eq H<sub>2</sub>O<sub>2</sub> (a) and PDT<sub>CN</sub> [2] + 8 eq H<sub>2</sub>O<sub>2</sub> (b) in MeCN.

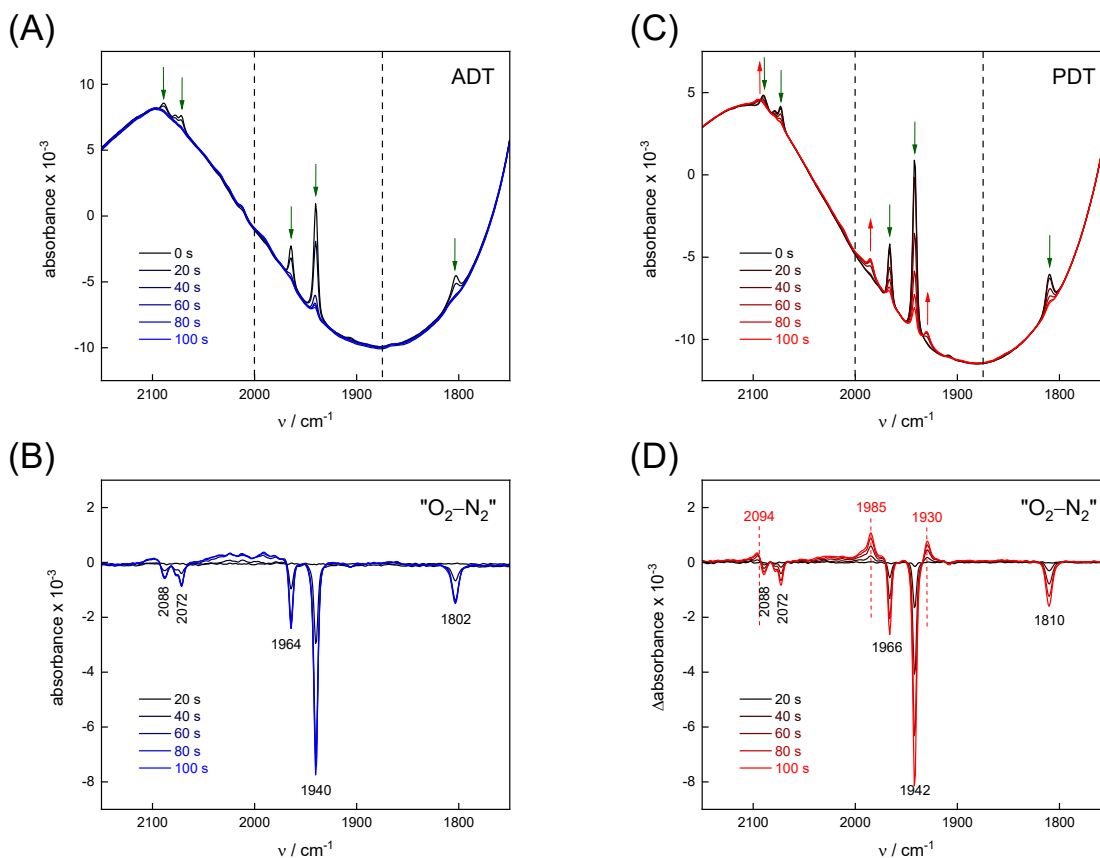
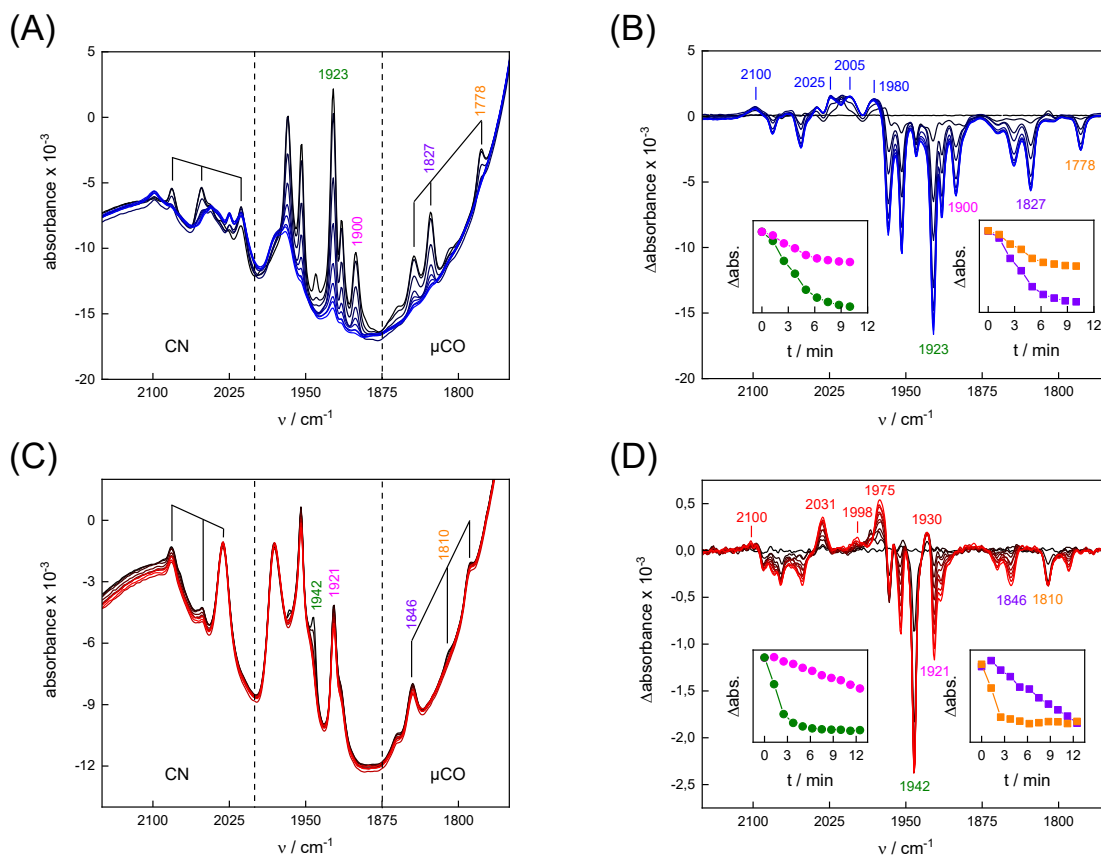


**Figure S10 |** Reactivity of *CrHydA1* cofactor variants activated with ADT<sub>CN</sub> [1] or PDT<sub>CN</sub> [2]. (A) Under N<sub>2</sub> (black traces), *CrHydA1*-ADT adopts the H<sub>ox</sub> state, whose CO/CN<sup>-</sup> band positions are marked. In the presence of 20% O<sub>2</sub>, the H-cluster disintegrates, and the bands disappear within ~2 minutes. (B) "O<sub>2</sub>-N<sub>2</sub>" difference spectra highlight the lack of positive bands that would indicate superoxidised intermediate species. (C) Under N<sub>2</sub> (black traces), *CrHydA1*-PDT adopts the H<sub>ox</sub> state, whose CO/CN<sup>-</sup> band positions are marked. In the presence of 20% O<sub>2</sub>, the H-cluster disintegrates, and the bands diminish within ~2 minutes. Note the gradual decrease of the bands as compared to (A). (D) "O<sub>2</sub>-N<sub>2</sub>" difference spectra highlight a set of positive bands that indicate the formation of an H-cluster fragment as discussed in the main script.



**Fig**

**ure S11 |** Reactions of CrHydA1 cofactor variants activated with ADT-monoCN (complex [3]) or PDT-monoCN (complex [4]) to 10% O<sub>2</sub>. Under N<sub>2</sub> (black traces), CrHydA1 ADT-monoCN (A) and PDT-monoCN (C) shows a variety of sharp bands in the CO/CN<sup>-</sup> regime, indicating successful maturation of the enzyme. Tentatively, we assign bands >2000 cm<sup>-1</sup> to cyanide stretching vibrations (CN<sup>-</sup>) and bands <1875 cm<sup>-1</sup> to the stretching vibrations of Fe-Fe bridging carbonyls (μCO). Intermediate band positions are assigned to terminal carbonyl vibrations (CO). Due to the presence of three main CN<sup>-</sup> bands and three main μCO bands under N<sub>2</sub>, a mixture of at least three different, unknown H-cluster states can be assumed. When O<sub>2</sub> is introduced to the headspace above the sample, large changes are observed for CrHydA1 ADT-monoCN (black-to-blue transition in (A)) while only minor oxidative damage is observed for CrHydA1 PDT-monoCN (black-to-red transition in (C)). (B) “O<sub>2</sub>-N<sub>2</sub>” difference spectra of CrHydA1 ADT-monoCN depict these changes more clearly. The vast majority of bands disappears (negative bands) and gives rise to a residual H-cluster population, characterized by high-frequency CO bands at 1980, 2005, and 2025 cm<sup>-1</sup> and a single CN<sup>-</sup> band at 2100 cm<sup>-1</sup>. In the example of the terminal CO bands at 1923 cm<sup>-1</sup> (green) and 1900 cm<sup>-1</sup> (magenta) or the μCO bands at 1827 cm<sup>-1</sup> (violet) and 1778 cm<sup>-1</sup> (orange) the decay can be followed over time (insets). (D) The vast majority of bands in “O<sub>2</sub>-N<sub>2</sub>” difference spectra of CrHydA1 PDT-monoCN disappears (negative bands) and gives rise to a residual H-cluster population, characterized by high-frequency CO bands at 1930, 1975, and 2031

$\text{cm}^{-1}$  and a single  $\text{CN}^-$  band at  $2100 \text{ cm}^{-1}$ . For the terminal CO bands at  $1942 \text{ cm}^{-1}$  (green) and  $1921 \text{ cm}^{-1}$  (magenta) or the  $\mu\text{CO}$  bands at  $1846 \text{ cm}^{-1}$  (violet) and  $1810 \text{ cm}^{-1}$  (orange) the decay can be followed over time (insets). These traces suggest faster, exponentially and slower, linearly decaying H-cluster intermediates. The reason for these kinetic differences is unclear; however, the data facilitates distinguishing different H-cluster species reacting with  $\text{O}_2$  at the same time.

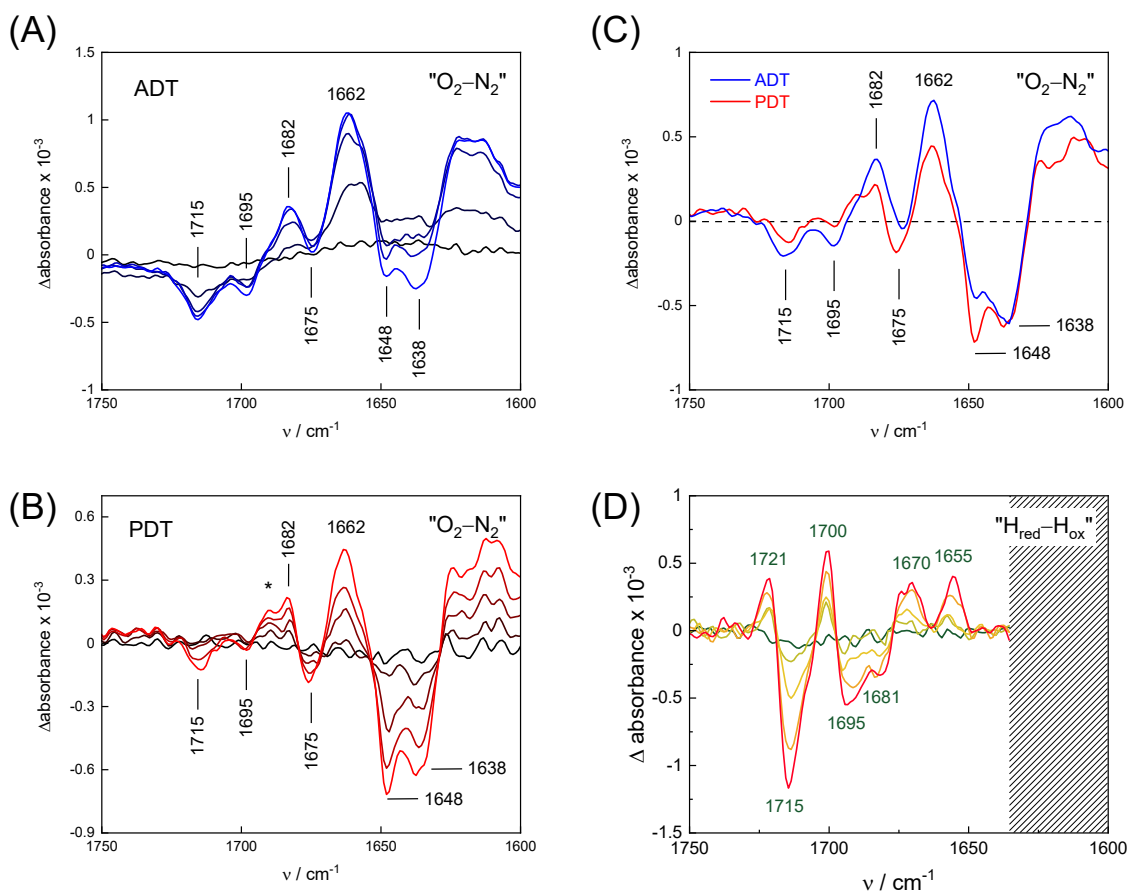


**Figure S12 |** Protonation changes upon  $\text{O}_2$ -induced degradation of  $\text{CrHydA1}$  wildtype ( $\text{ADT}_{\text{CN}}$ ) and cofactor variant  $\text{PDT}_{\text{CN}}$ . Evolution of FTIR difference spectra between  $1750\text{--}1600 \text{ cm}^{-1}$  over time for  $\text{CrHydA1}^{\text{adt}}$  (A) and  $\text{CrHydA1}^{\text{pdt}}$  (B). Comparison of the final spectra as shown in the main script (C), and a comparison of FTIR difference spectra record for the reduction of  $\text{H}_{\text{ox}}$  into  $\text{H}_{\text{red}}$  as published previously (D).<sup>[7]</sup> Glutamic acid marker bands at  $1715$  and  $1700 \text{ cm}^{-1}$  are negative in panel (C) indicating deprotonation of E141 in the proton transfer pathway, while the arginine band at  $1682 \text{ cm}^{-1}$  is positive, which results from the protonation of R148. Clear protonation changes involving E144 ( $1721$  and  $1695 \text{ cm}^{-1}$ ) are not detected. Difference features below  $1675 \text{ cm}^{-1}$  are assigned to secondary structural changes.<sup>[8]</sup>

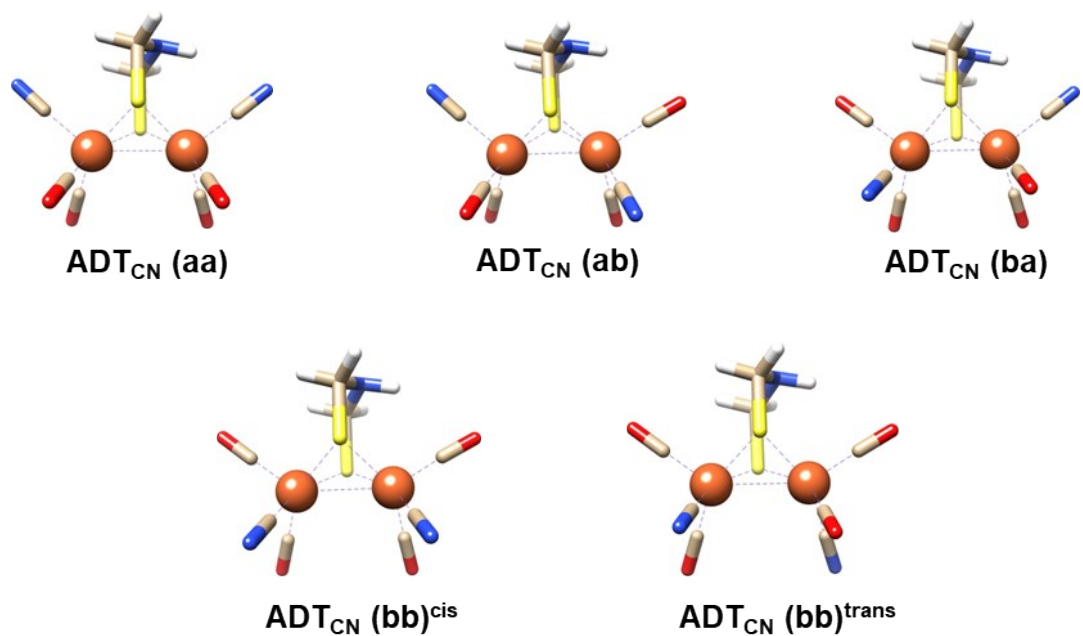


**Figure S13** | Five possible structural isomers of  $\text{ADT}_{\text{CN}}$  [1] with respect to apical and basal positions of  $\text{CN}^-$  ligands.

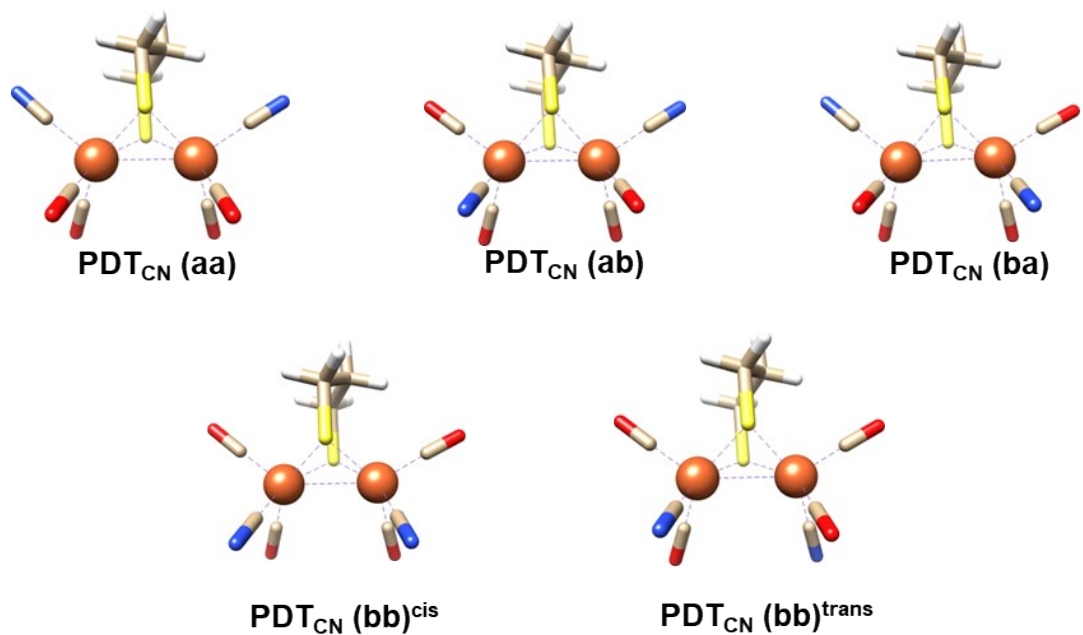


**Figure S14** | Five possible structural isomers of  $\text{PDT}_{\text{CN}}$  [2] with respect to apical and basal positions of  $\text{CN}^-$  ligands.

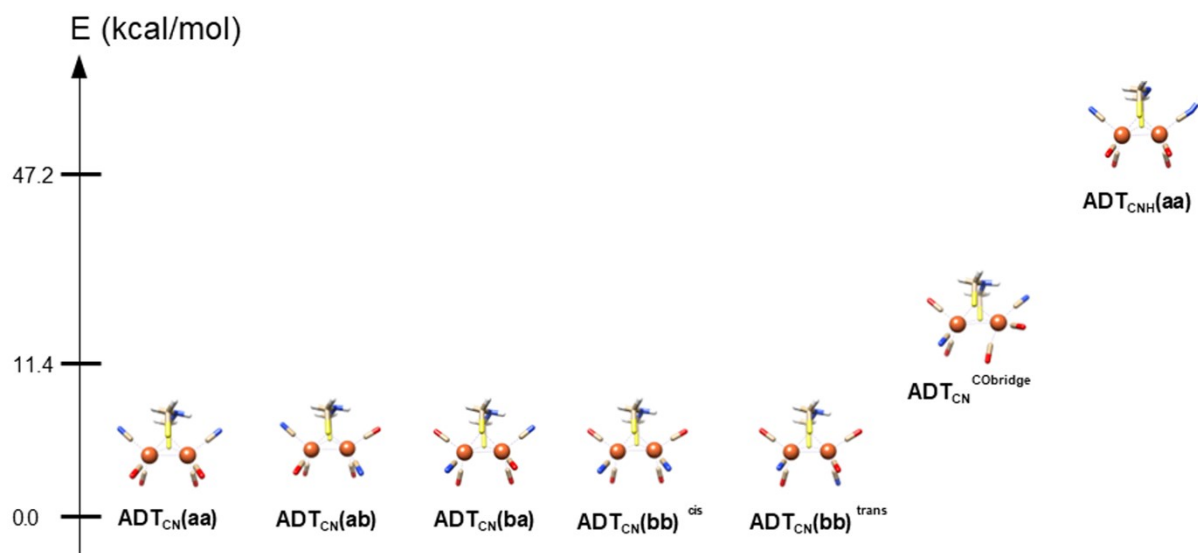


Figure S15 | Relative Gibbs free energies of the structural isomers of  $\text{ADT}_{\text{CN}}$  [1].

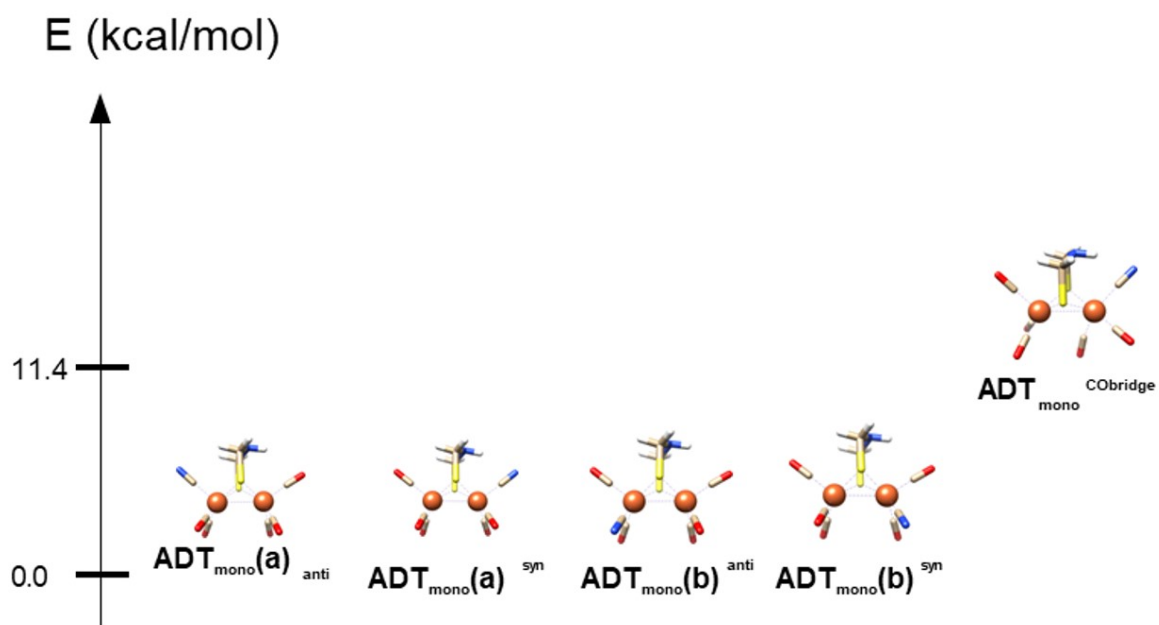
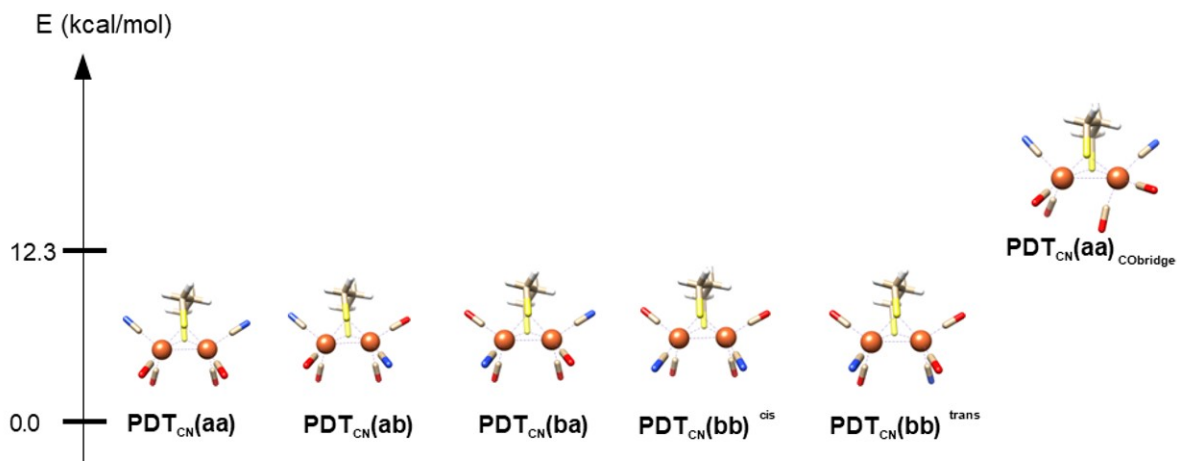
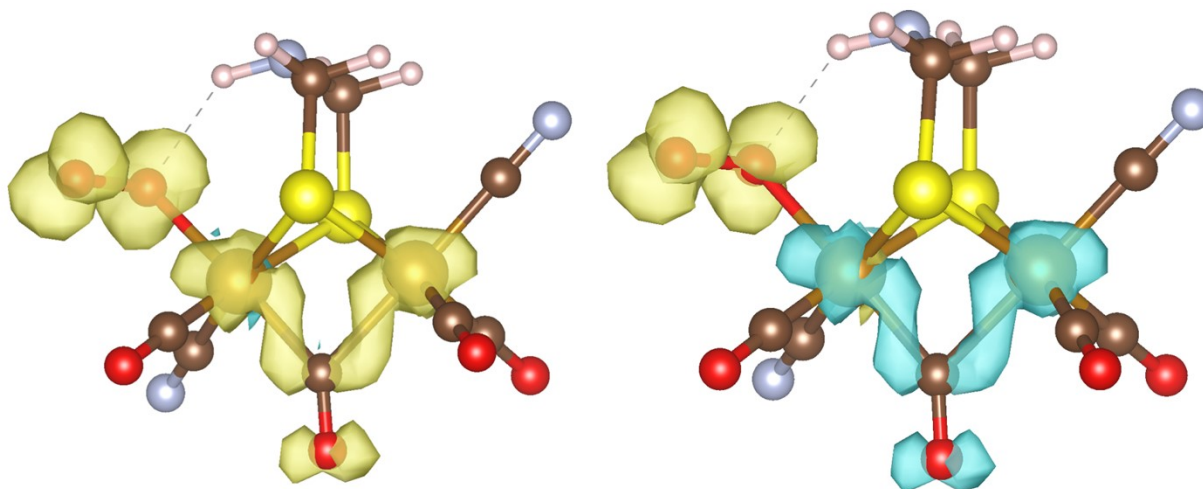


Figure S16 | Relative Gibbs free energies of the structural isomers of  $\text{ADT}_{\text{monoCN}}$  [3].



**Figure S17** | Relative Gibbs free energies of the structural isomers of PDT<sub>CN</sub> [2].



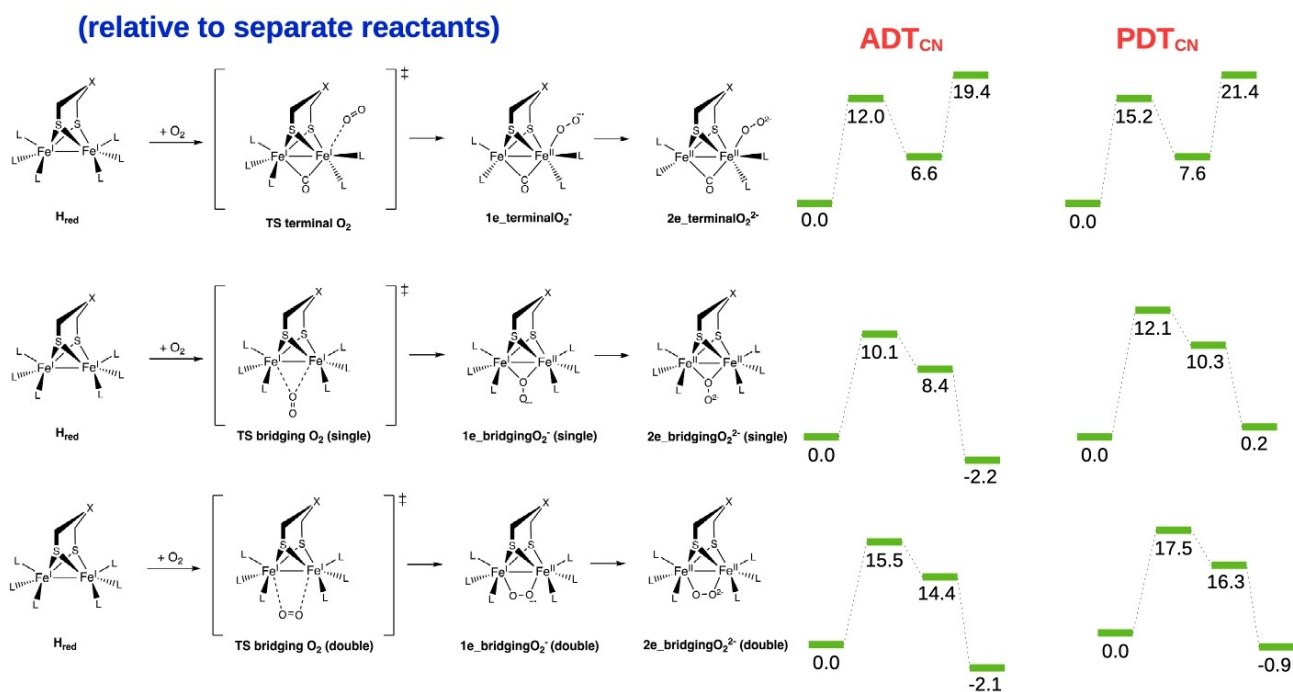
**Figure S18** | Spin isodensity plots for the one-electron reduced oxygenated products. Both ferromagnetic (left) and antiferromagnetic coupling (right) of the two radicals were modelled.

### The oxygenated state

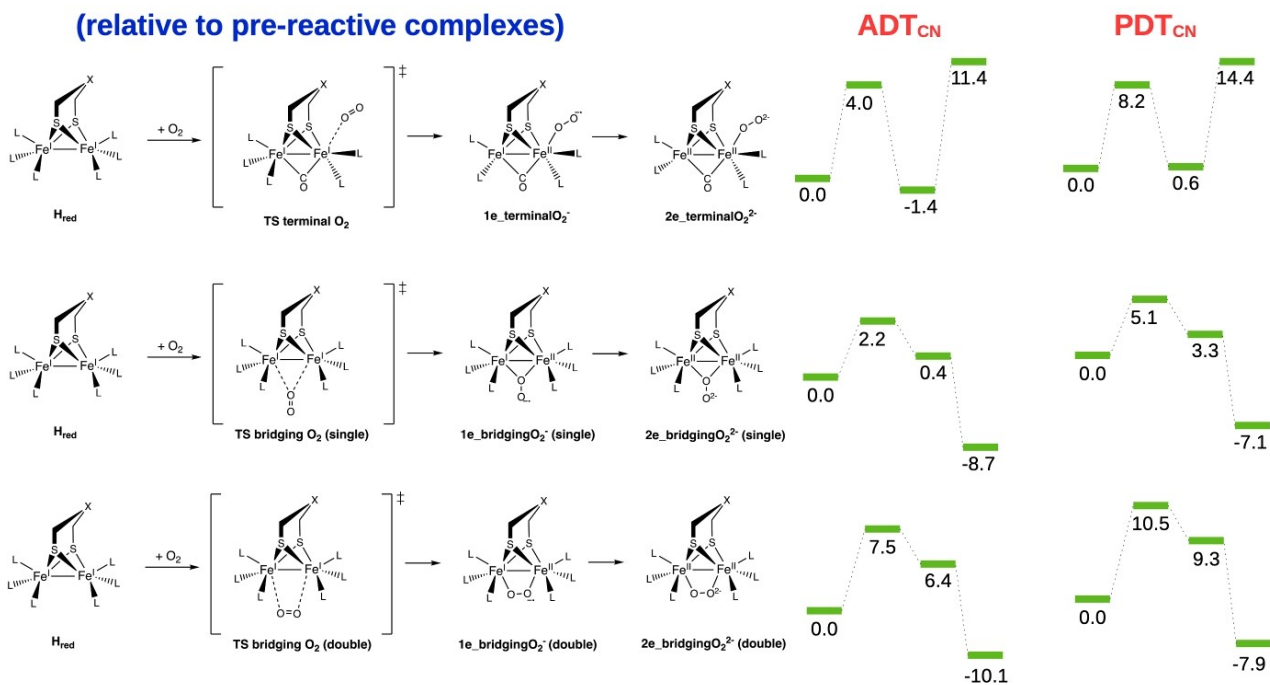
The oxygenation reaction has been considered in three main routes as shown in **Figure S19–S20**. An end-on binding and a bridging mode with either single or dual binding mode were modelled. The same barriers have been calculated relative to both separate reactants and pre-reactive complexes (PRCs), as oxygenated products suffer from loss of translational entropy which is known to be overestimated in quantum chemical calculations of the presented type. Following the transition state, one- and two-electron processes of oxygenated products were modeled and denoted with the prefixes “1e-” and “2e-” in the reaction profiles.

If one electron is transferred from the Fe cluster to  $O_2$ , resulting  $Fe^{II}-Fe^I$  superoxo complex features two unpaired electrons whose spins can couple ferromagnetically and antiferromagnetically, thus leading to a spin triplet or singlet, respectively. Both of these scenarios were considered and successfully located at the DFT (or BSDFT) level, and the spin isodensity plots are given in the figure below. The antiferromagnetically coupled state was found to be 1.2 kcal/mol less stable.

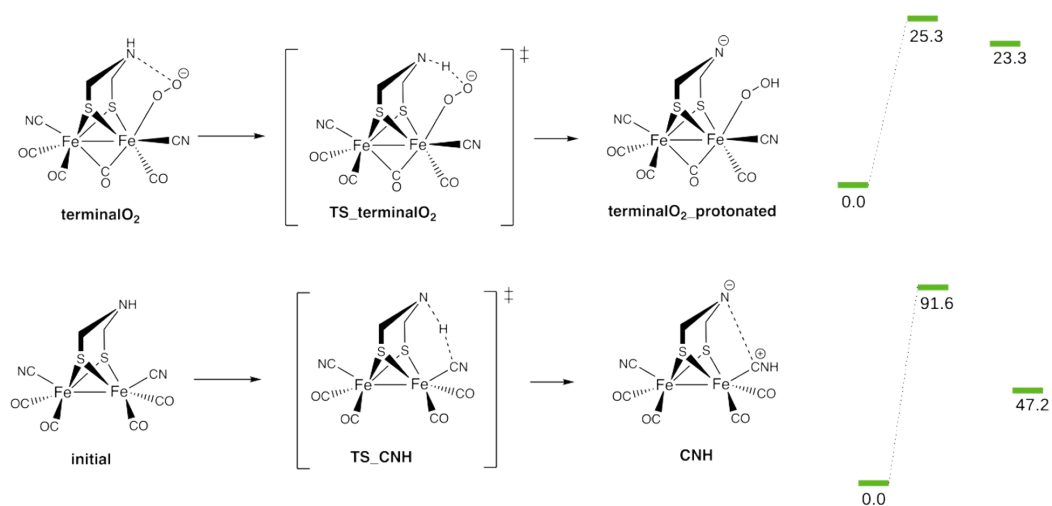
Transfer of two electrons to oxygen yields a complex with a  $Fe^{II}-Fe^{II}$  oxidation state, accompanied by the formation of a peroxide dianion  $O_2^{2-}$ , which refers to a closed shell system. The Gibbs free energy profiles of oxygenation reactions referenced either to separate reactants and pre-reactive complexes (PRCs) are given in the following figures. For all different oxygen attack modes, complex **[1]** exhibited a lower activation barrier, approximately 2-3 kcal/mol lower than that of complex **[2]**. The one electron reduced complexes were observed to be reactive intermediates. In comparison to the bridging coordination mode of oxygen, which results in a thermodynamic product of peroxide dianion nature, the terminal coordination of oxygen was determined to be thermodynamically unfeasible.



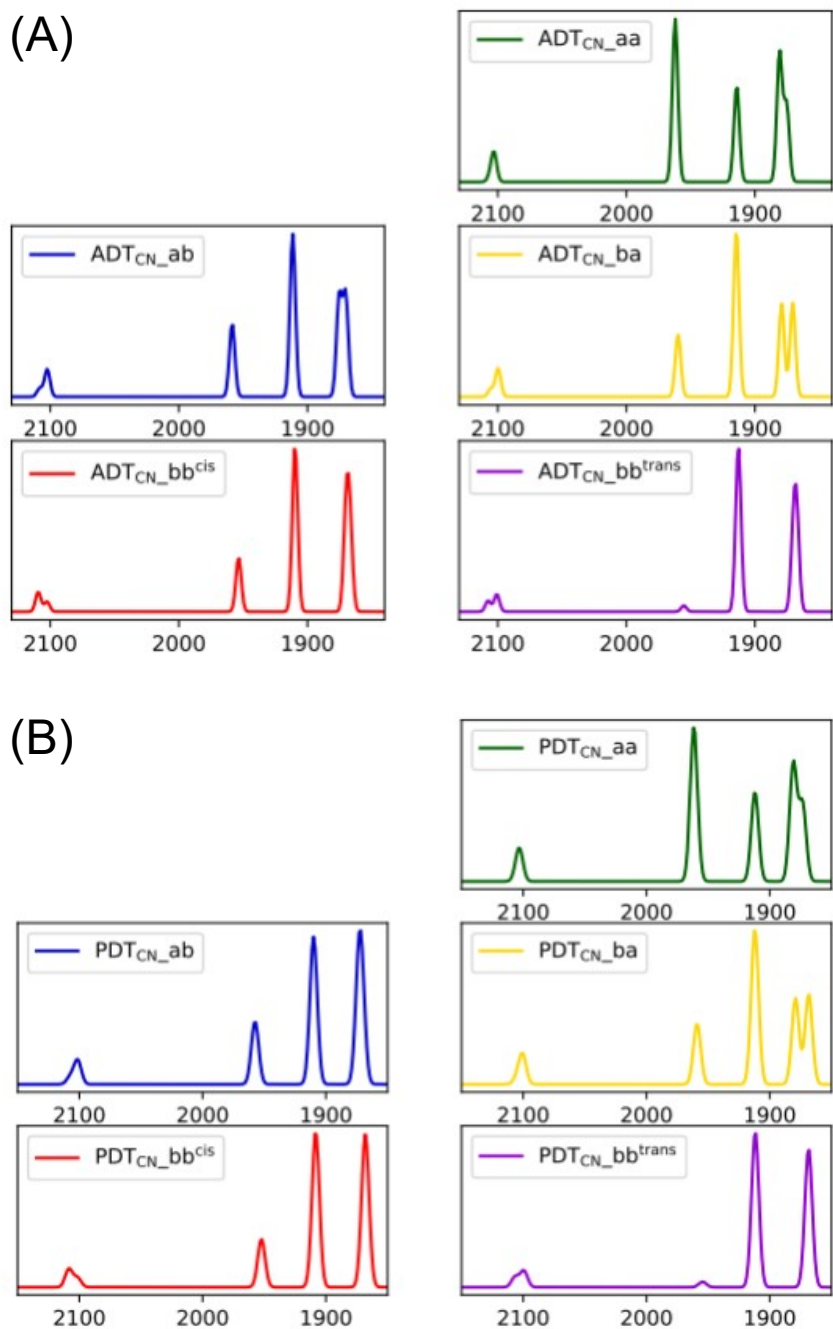
**Figure S19** | Oxygenation reaction coordinate for  $XDT_{CN}$ . The Gibbs free energies were calculated relative to the infinitely separated hydrogenase and  $O_2$  moieties.



**Figure S20** | Oxygenation reaction coordinate for XDT<sub>CN</sub>. The Gibbs free energies were calculated relative to the pre-reactive complexes (PRCs), in which both the model complexes and the O<sub>2</sub> moieties are in the same solvent cavity.

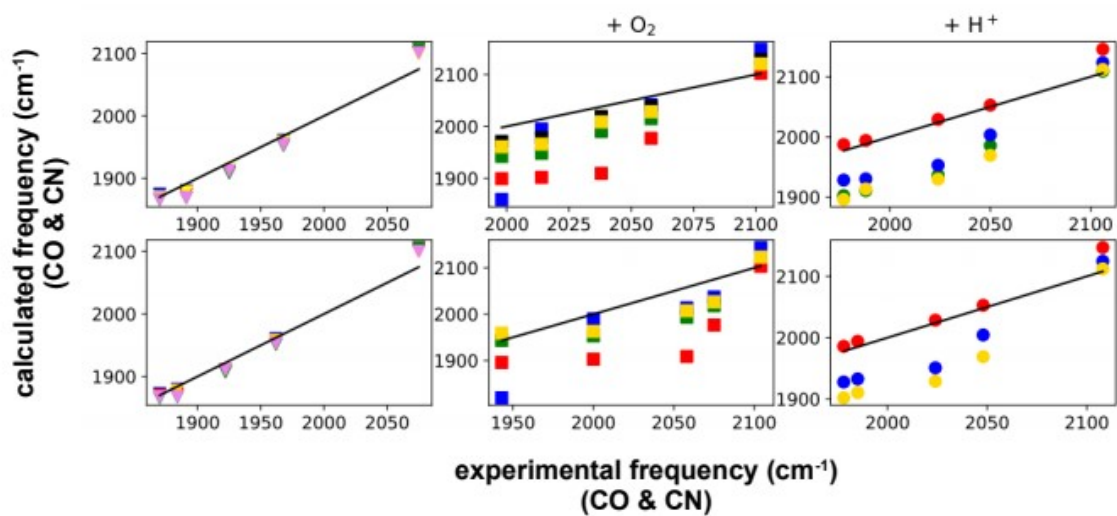


**Figure S21** | Depiction of calculations of reactions involving the interaction of the incoming oxygen and the bridgehead proton in ADT<sub>CN</sub> [1].



**Figure S22** | Calculated IR spectra for ADT<sub>CN</sub> [1] (A) and PDT<sub>CN</sub> [2] (B) while considering different

structural isomers. A scaling factor of 0.978 has been applied. See Figure S13–14 for the nomenclature.



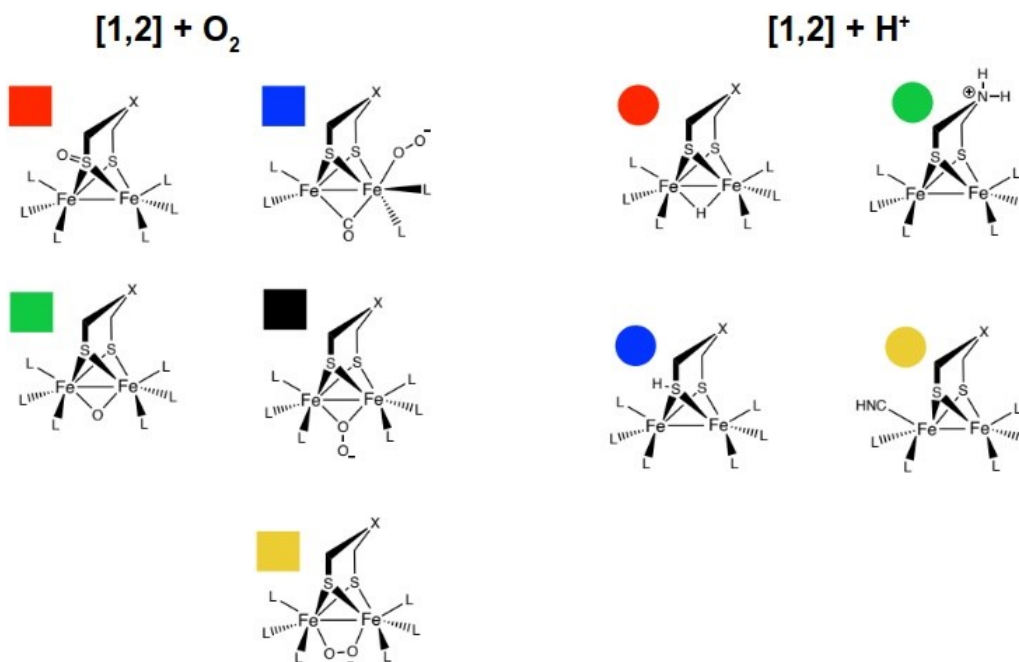


**Figure S23** | Correlation between experimentally observed and predicted CO and CN stretching frequencies for ADT<sub>CN</sub> **[1]** and PDT<sub>CN</sub> **[2]**. The colors encode the different possible species after oxygenation and protonation. The scaling factor 0.978 has been determined using both CO and CN vibrations.

### Comparison between experimental and calculated IR spectra

**Figure S22** depicts the effect of structural isomerism of CN and CO ligands on the IR frequencies. As per the lineshape of the CO-frequency region, the highest similarity between the experimental and calculated spectra is observed when both of the CN groups are on apical positions.

A correlation analysis of the experimental and calculated infrared spectra was conducted as shown in **Figure S23**. Herein, the x and y axes represent the experimental and calculated CO vibrations, respectively. The subplots involve the initial state of the substrate, the oxygenated and hydrogenated products. The colors encode the different possible species after oxygenation and protonation. The oxygenated products in this figure involve the two-electron reduced complexes, as they exhibited the closest agreement with the experimental spectra.

The apical-basal isomerism of CN-ligands did not induce a noticeable variance in the CO vibrations for either complex **[1]** or **[2]**. The correlation between the experiment and calculated spectra in

the presence of oxygen was found to be the best when the oxygen is bound to the substrate in a bridging mode (depicted as black and orange) as can be seen in Figure S24. Similarly, the best agreement is observed for the hydrogenated product when a bridging hydride (shown in red) is formed.

A comprehensive list of all simulated species, alongside the corresponding experimental data is presented in **Table S4–S5**. The experimental CO-peak position difference for  $\text{XDT}_{\text{CN}}\text{-O}_2$  and  $\text{XDT}_{\text{CN}}\text{+O}_2$  has been noted as Exp. diff. Similarly, the peak positional change has been recorded for calculated IR spectra too, to have a better comparison between calculated and experimental spectra. Oxygenation at one of the sulfur atoms did not bring about a noticeable difference in the CO-vibration regime as compared to the initial  $\text{XDT}_{\text{CN}}\text{-O}_2$  system. This outcome was anticipated given that the coordination environment of the iron centers was not markedly altered in this binding mode. A terminal coordination of the  $\text{O}_2$  moiety in all cases result in a highly asymmetric shift of CO-vibrations, which is not in line with the experimentally observed differences. Considering the reaction profiles (see previous section) along with the IR data, it can be inferred that a terminal binding of oxygen is highly unlikely. The bridging coordination of the peroxide dianion to  $\text{Fe}^{\text{II}}\text{-Fe}^{\text{II}}$  obtained by a two-electron process exhibits the closest agreement with the experimental data, characterized by a progressively positive shift of approximately  $90\text{ cm}^{-1}$  on average.

## Tables

**Table S1** | Comparison of isomer shift and quadrupole splitting of complexes **[1]** and **[2]** with 8 equivalents of H<sub>2</sub>O<sub>2</sub>.

	<b>[1]</b>	<b>[1]</b>		<b>[2]</b>	<b>[2]</b>	
	Fe1	Fe1	Fe2	Fe1	Fe1	Fe2
<b>treatment</b>	<b>-H<sub>2</sub>O<sub>2</sub></b>	<b>+H<sub>2</sub>O<sub>2</sub></b>		<b>-H<sub>2</sub>O<sub>2</sub></b>	<b>+H<sub>2</sub>O<sub>2</sub></b>	
<b>δ</b>	0.037	0.237	0.352	0.035	0.195	0.240
<b>ΔE<sub>q</sub></b>	1.109	0.182	0.963	0.951	0.299	1.180
<b>treatment</b>	<b>-O<sub>2</sub></b>	<b>+O<sub>2</sub></b>		<b>-O<sub>2</sub></b>	<b>+O<sub>2</sub></b>	
<b>δ</b>	0.037	0.238	0.345	0.035	0.204	0.358
<b>ΔE<sub>q</sub></b>	1.109	0.253	1.188	0.951	0.288	1.219

**Table S2** | Comparison of the  $\nu_{\text{CO}}$  in the FTIR spectra of the model complexes investigated in this work **[1-4]** vs the previously reported H-cluster models **[5-8]** with varied ligand systems.<sup>[5,6]</sup> FTIR values mentioned before and after oxygenation. Values in italics refer to  $\nu_{\text{CN}^-}$  in complexes **[1-4]**.

Oxidising conditions	$O_2$ (this work)				$e^- + O_2$		<i>m</i> -CPBA	
	ADT <sub>CN</sub> [1] (MeCN)	PDT <sub>CN</sub> [2] (MeCN)	ADT <sub>mono-CN</sub> [3] (MeCN)	PDT <sub>mono-CN</sub> [4] (MeCN)	ADT <sub>CO</sub> [5] (DCM)	PDT <sub>CO</sub> [6] (DCM)	PDT <sub>(CO)5(PPh3)</sub> [7] (MeCN)	PDT <sub>(CO)4(PPh3)2</sub> [8] (MeCN)
Before oxidation	2075 1968 1925 1891 1870	2075 1962 1922 1884 1870	2092 2033 1975 1956 1944 1915	2092 2030 1975 1956 1944 1915	2074 2033 2000 1989	2074 2033 2000 1989	2044 1982 1931	1979 1942 1898
After oxidation	2102 2058 2038 2014 1998	2104 2075 2058 2000 1934			2038 1997 1957 1946	2020 1960 1891 1950-1910 br, sh	2056 1998 1971 1953	1994 1985 1958 1917
Site of oxygenation	iron		?		sulfur		sulfur	

**Table S3 |** Overview of the  $\nu_{\text{CO}}$  and  $\nu_{\text{CN}^-}$  in the FTIR spectra of CrHydA1 variants with and without treatment with oxygen. References denote the values taken from the FTIR spectra reported in the literature. For all variants CrHydA1<sup>adt</sup> and CrHydA1<sup>pd</sup>t the samples were purged with N<sub>2</sub> before treatment with O<sub>2</sub> to accumulate the H<sub>ox</sub> state. Notably, after treatment with O<sub>2</sub>, the CrHydA1<sup>mono-adt</sup> variant shows distinct changes while the spectra of CrHydA1<sup>mono-pdt</sup> remains relatively unaltered.

CrHydA1	adt	adt	pd	pd	mono-adt	mono-adt	mono-pdt	mono-pdt
	H <sub>ox</sub> <sup>[21]</sup>	H <sub>ox</sub> + O <sub>2</sub>	H <sub>ox</sub> <sup>[22]</sup>	H <sub>ox</sub> + O <sub>2</sub>	?	? + O <sub>2</sub>	?	? + O <sub>2</sub>
$\nu_{\text{CN}^-}$	2088		2090		2080		2082	
	2070		2073	2095	2053	2100	2050	
					2013		2031	
$\nu_{\text{CO}}$					1967		1980	
	1964		1965		1954		1965	
				1985	1939	2025	1959	
	1940		1941		1923	2005	1942	
				1930	1914	1980	1921	
					1900			
$\mu_{\text{CO}}$					1844		1859	
					1827		1846	
	1802		1810		1778		1810	
							1788	

*\*Direct annotation of H-cluster state in case of CrHydA1<sup>mono-adt</sup> and CrHydA1<sup>mono-pdt</sup> cannot be done, as multiple bands originating from mixture of states are present. Although the samples were purged with N<sub>2</sub> before treatment with O<sub>2</sub>, the multiple signals can be attributed to two different isomers of mono-CN models maturing the apo-HydA1.<sup>[23]</sup> Additionally, some contamination from the di-CN cofactor might be present.*

**Table S4** | ADT<sub>CN</sub> oxygenation. The experimental CO and CN-peak position difference for XDT<sub>CN</sub><sup>-</sup>O<sub>2</sub> and XDT<sub>CN</sub>+O<sub>2</sub> has been noted as Exp. diff. Similarly, the peak positional change has been recorded for calculated IR spectra too, to have a better comparison between calculated and experimental spectra. A scaling factor of 0.978 has been used for the calculated frequencies.

ADT <sub>CN</sub> [1]	CO	CO	CO	CO	CN
(aa)	1875.4	1880.9	1914.2	1962.1	2103.5
<b>exp. diff.</b>	128.0	123.0	113.0	90.0	27
1e_terminal O <sub>2</sub>	1767.6	1964.6	1977.1	2020.0	2133.9
<b>difference</b>	-107.8	83.7	62.9	57.9	30.4
2e_terminal O <sub>2</sub>	1860.2	1996.1	2014.1	2042.7	2149.7
<b>difference</b>	-15.3	115.2	99.9	80.7	46.2
1e_bridging O <sub>2</sub> single	1864.1	1942.2	1991.0	2041.9	2114
<b>difference</b>	-11.3	61.3	76.8	79.8	10.5
2e_bridging O <sub>2</sub> single	1971.7	1979.0	2020.2	2039.3	2129.8
<b>difference</b>	96.3	98.1	105.9	77.3	26.3
1e_bridging O <sub>2</sub> double	1854.6	1931.2	1987.4	2039.0	2111.73
<b>difference</b>	-20.8	50.3	73.2	77.0	8.2
2e_bridging O <sub>2</sub> double	1961.9	1966.9	2009.7	2029.3	2122.92
<b>difference</b>	86.5	86.0	95.5	67.2	19.4
bridging O	1943.1	1949.2	1991.2	2015.8	2118
<b>difference</b>	67.7	68.3	77.0	53.7	14.5
sulphur O	1900.2	1902.8	1910.3	1977.9	2103.3
<b>difference</b>	24.7	21.9	-3.9	15.8	-0.2

**Table S5** | PDT<sub>CN</sub> oxygenation. The experimental CO and CN-peak position difference for XDT<sub>CN</sub><sup>-</sup>O<sub>2</sub> and XDT<sub>CN</sub>+O<sub>2</sub> has been noted as Exp. diff. Similarly, the peak positional change has been recorded for calculated IR spectra too, to have a better comparison between calculated and experimental spectra. A scaling factor of 0.978 has been used for the calculated frequencies. A bridging O<sub>2</sub> on [2] in a single coordination mode could not be located.

PDT <sub>CN</sub> [2]	CO	CO	CO	CO	CN
(aa)	1873.4	1880.9	1912.1	1961.5	2103.2
<b>exp. diff.</b>	73.0	116.0	136.0	113.0	29
1e_terminal O <sub>2</sub>	1732.9	1931.6	1942.9	1986.3	2133.2
<b>difference</b>	-140.4	50.8	30.8	24.8	30.0
2e_terminal O <sub>2</sub>	1820.4	1990.7	2014.7	2038.1	2144.8
<b>difference</b>	-53.0	109.8	102.6	76.6	15.0
1e_bridging O <sub>2</sub> single	1833.0	1910.5	1957.3	2008.0	2118.2
<b>difference</b>	-40.4	29.6	45.2	46.6	15.0
1e_bridging O <sub>2</sub> double	1823.2	1899.1	1953.1	2005.0	2114.4
<b>difference</b>	-50.2	18.2	41.0	43.5	11.2
2e_bridging O <sub>2</sub> double	1960.0	1963.8	2008.1	2027.6	2123.8
<b>difference</b>	86.7	82.9	96.0	66.1	20.6
bridging O	1944.3	1954.0	1994.1	2019.1	2122.5
<b>difference</b>	70.9	73.2	82.1	57.6	19.3
sulphur O	1896.6	1903.7	1909.5	1977.5	2104.2
<b>difference</b>	23.3	22.8	-2.5	16.0	1.0

**Table S6** | Crystal data and structure refinement for Fe<sub>2</sub>(adt<sup>Cbz</sup>)(CO)<sub>6</sub>

Data	
Empirical formula	C <sub>14.22</sub> H <sub>9.78</sub> Fe <sub>1.78</sub> N <sub>0.89</sub> O <sub>7.11</sub> S <sub>1.78</sub>
Temperature (K)	105(9)
Crystal system	monoclinic
Space group	I2/a
a (Å)	18.4651(3)
b (Å)	7.39098(15)
c (Å)	29.6260(5)
α (°)	90
β (°)	101.6865 (17)
γ (°)	90
Volume (Å <sup>3</sup> )	3959.41(12)
Z	9
Density, ρ <sub>calc</sub> (g/cm <sup>3</sup> )	1.748
Absorption coefficient μ (mm <sup>-1</sup> )	1.720
F(000)	2096.0
Radiation	Cu Kα (λ = 1.54184)
2θ range for data collection/°	2.808 to 53.542
Index ranges	-23 ≤ h ≤ 21, -8 ≤ k ≤ 9, -25 ≤ l ≤ 36
Reflections collected	14462
Independent reflections	4081 [R <sub>int</sub> = 0.0378, R <sub>sigma</sub> = 0.0288]
Data/restraints/parameters	4081/0/306
Goodness-of-fit on F <sup>2</sup>	1.135
Final R indexes [I ≥ 2σ (I)]	R <sub>1</sub> = 0.0451, wR <sub>2</sub> = 0.1168
Final R indexes [all data]	R <sub>1</sub> = 0.0487, wR <sub>2</sub> = 0.1187
Largest diff. peak/hole (e Å <sup>-3</sup> )	0.61/-0.76

## References

- [1] C. Sommer, C. P. Richers, W. Lubitz, T. B. Rauchfuss, E. J. Reijerse, *Angewandte Chemie International Edition* **2018**, *57*, 5429–5432.
- [2] A. P. G. Kieboom, *Recueil des Travaux Chimiques des Pays-Bas* **1988**, *107*, 685–685.
- [3] S. T. Stripp, *ACS Catal.* **2021**, *11*, 7845–7862.
- [4] J. Esselborn, C. Lambertz, A. Adamska-Venkatesh, T. Simmons, G. Berggren, J. Noth, J. Siebel, A. Hemschemeier, V. Artero, E. Reijerse, M. Fontecave, W. Lubitz, T. Happe, *Nat Chem Biol* **2013**, *9*, 607–609.
- [5] V. C.-C. Wang, C. Esmieu, H. J. Redman, G. Berggren, L. Hammarström, *Dalton Trans.* **2020**, *49*, 858–865.
- [6] T. Liu, B. Li, M. L. Singleton, M. B. Hall, M. Y. Darensbourg, *J. Am. Chem. Soc.* **2009**, *131*, 8296–8307.
- [7] M. Senger, V. Eichmann, K. Laun, J. Duan, F. Wittkamp, G. Knör, U.-P. Apfel, T. Happe, M. Winkler, J. Heberle, S. T. Stripp, *J. Am. Chem. Soc.* **2019**, *141*, 17394–17403.
- [8] A. Barth, *Biochimica et Biophysica Acta (BBA) - Bioenergetics* **2007**, *1767*, 1073–1101.
- [9] F. Neese, *WIREs Computational Molecular Science* **2018**, *8*, e1327.
- [10] A. D. Becke, *J. Chem. Phys.* **1993**, *98*, 5648–5652.
- [11] F. Weigend, *Phys. Chem. Chem. Phys.* **2006**, *8*, 1057–1065.
- [12] E. van Lenthe, E. J. Baerends, J. G. Snijders, *J. Chem. Phys.* **1993**, *99*, 4597–4610.
- [13] E. van Lenthe, E. J. Baerends, J. G. Snijders, *J. Chem. Phys.* **1994**, *101*, 9783–9792.
- [14] C. van Wüllen, *J. Chem. Phys.* **1998**, *109*, 392–399.
- [15] B. I. Dunlap, J. W. D. Connolly, J. R. Sabin, *J. Chem. Phys.* **1979**, *71*, 3396–3402.
- [16] O. Vahtras, J. Almlöf, M. W. Feyereisen, *Chemical Physics Letters* **1993**, *213*, 514–518.
- [17] F. Neese, F. Wennmohs, A. Hansen, U. Becker, *Chemical Physics* **2009**, *356*, 98–109.
- [18] R. Izsák, F. Neese, *J. Chem. Phys.* **2011**, *135*, 144105.
- [19] R. Izsák, F. Neese, W. Klopper, *J. Chem. Phys.* **2013**, *139*, 094111.
- [20] D. A. Pantazis, X.-Y. Chen, C. R. Landis, F. Neese, *J. Chem. Theory Comput.* **2008**, *4*, 908–919.
- [21] M. Winkler, M. Senger, J. Duan, J. Esselborn, F. Wittkamp, E. Hofmann, U.-P. Apfel, S. T. Stripp, T. Happe, *Nat Commun* **2017**, *8*, 16115.
- [22] M. Senger, K. Laun, F. Wittkamp, J. Duan, M. Haumann, T. Happe, M. Winkler, U.-P. Apfel, S. T. Stripp, *Angewandte Chemie International Edition* **2017**, *56*, 16503–16506.
- [23] M. Lorenzi, J. Gellert, A. Zamader, M. Senger, Z. Duan, P. Rodríguez-Maciá, G. Berggren, *Chemical Science* **2022**, *13*, 11058–11064.